Journal of the Brazilian Society of Mechanical Sciences and Engineering (2020) 42:378
https://doi.org/10.1007/s40430-020-02453-9

TECHNICAL PAPER

Numerical analysis of the influence of magnetic field waveforms on the performance of active magnetic regenerators

Fábio P. Fortkamp[1] · Gusttav B. Lang[1] · Jaime A. Lozano[1] · Jader R. Barbosa Jr[1]

Received: 12 November 2019 / Accepted: 5 June 2020 / Published online: 26 June 2020

Abstract
Magnetic cooling is an alternative to vapor compression that does not rely on the use of hazardous substances. The refrigerant is a solid material which reacts to oscillations in magnetic field by changing its temperature (the magnetocaloric effect). In active magnetic regenerators, the magnetocaloric material arranged as a porous medium is subjected to an oscillating fluid flow to allow heat transfer from a cold source to a hot sink in a thermodynamic cooling cycle. Although the literature is abundant with studies on the influence of the fluid flow waveform on magnetic refrigeration devices, the influence of the magnetic field waveform has been much less investigated. In this work, we make use of an active magnetic regenerator numerical model with different mathematically defined waveforms to determine which operating parameters yield the highest values of cooling capacity and coefficient of performance for a specific set of operating conditions. The results show that the best performance is achieved when the magnetic field is kept constant for the same time duration of the fluid flow through the magnetized material, and the transition times between the high and low levels of the magnetic field should be as short as possible.

Keywords Magnetic refrigeration · Active magnetic regenerator · Numerical modeling · Magnetocaloric effect

List of symbols

Variables

A_t	Amplitude of the pressure gradient waveform in the fluid momentum equation $(\mathrm{m/s^2})$
B	Magnetic flux density (T)
c	Specific heat (J/(kg K))
c_E	Ergun constant of the porous medium
COP	Coefficient of performance
D_{ld}	Dispersion term in the AMR model $(\mathrm{m/s^2})$
D_p	Particle diameter (m)
f	Cycle frequency (Hz)
F_B	Blow Fraction
F_M	Magnetization fraction
$g(t)$	Dimensionless waveform of the pressure gradient term in the fluid momentum equation
$\hbar$	Heat transfer coefficient $(\mathrm{W/(m^2K)})$
H	Magnetic field (H)
h	Thickness (m)
H_{reg}	Regenerator height (m)
K	Permeability of the porous medium $(\mathrm{m^2})$
k	Thermal conductivity (W/(mK))
L_{reg}	Regenerator length (m)
$\dot{m}_f$	mass flow rate (kg/s)
M	Magnetization field (H)
m	Mass (kg)
N_D	Demagnetization factor
N_{reg}	Number of regenerators
N_{valve}	Number of valves
ΔP	Total pressure drop across one regenerator (Pa)
P	Pressure (Pa)
$\dot{Q}_C$	Cooling capacity (W)
$\dot{q}_{csg}$	Volumetric casing losses in the AMR model $(\mathrm{W/m^3})$
ΔT_{ad}	Adiabatic temperature variation (K)
T	Temperature (K)

An abridged version of this manuscript was presented at the 24th ABCM International Congress of Mechanical Engineering (COBEM 2017), held in Curitiba, PR, Brazil, in December 2017.

Technical Editor: Jose A. R. Parise.

✉ Jader R. Barbosa Jr
jrb@polo.ufsc.br

[1] POLO — Research Laboratories for Emerging Technologies in Cooling and Thermophysics, Department of Mechanical Engineering, Federal University of Santa Catarina, Florianópolis, SC 88040-900, Brazil

t	Time (s)
V	Velocity (m/s)
W_{reg}	Regenerator width (m)
$\dot{W}_{mag}$	Magnetic power (W)
$\dot{W}_{pump}$	Pumping power (W)
$\dot{W}_{valve,n}$	Nominal power consumption of one valve (W)
$\dot{W}_{valve}$	Valve power (W)
$\dot{W}_{relay,n}$	Nominal power consumption of one relay (W)
x, y, z	Coordinate system variables (m)

Greek symbols

β	Surface area density (m^2/m^3)
ε	Porosity
Φ	Utilization factor
η_{2nd}	Second-law efficiency
$\tan \theta_R$	Ramp rate in the magnetic ramp profile (T/s)
ρ	Density (kg/m^3)
τ	Time period (s)
$\tau_{0,CC}, \tau_{0,HC}$	Time periods without fluid flow in the respective half-cycle (see list of Abbreviations) (s)
τ_B	Blow duration (s)
τ_M	Magnetization period in the magnetic ramp profile (s)
τ_R	Ramp period in the magnetic ramp profile (s)
μ_f	Fluid dynamic viscosity (Pa s)
μ_0	Magnetic permeability of free space (H/m)

Subscripts and superscripts

air	Air layer between magnets and regenerators
csg	Regenerator casing
eff	Effective
f	Fluid phase
p	Constant-pressure
s	Solid phase
sf	Relative to the heat transfer between solid and fluid phases in the regenerator
x	Yttrium fraction

Abbreviations

AMR	Active Magnetic Regenerator
C	Cold source
CB	Cold blow
CC	Cold cycle
CE	Cold end
H	Hot source
DoE	Design of experiments
HB	Hot blow
HC	Hot cycle
IT	Instantaneous magnetic profile
MCE	Magnetocaloric effect
MCM	Magnetocaloric material
MR	Magnetic (or magnetocaloric) refrigeration
RC	Rectified cosine magnetic profile
RM	Ramp magnetic profile

1 Introduction

Although mechanical vapor compression has been the dominant cooling technology for the past century [1], it still faces a number of challenges related to its environmental footprint. For instance, the phase-out of refrigerants with ozone depleting and global warming potentials brought about a more widespread use of flammable substances, which pose a new set of concerns, restrictions and additional technological challenges for consumer applications [2, 3].

Magnetic refrigeration (MR) is an emerging cooling technology which does not rely on hazardous fluids. In MR, the temperature of a *magnetocaloric material* (MCM) changes as a result of cyclical changes in the applied magnetic field due to the so-called *magnetocaloric effect* (MCE). The magnitude of the MCE depends on material properties, magnetic field variation and temperature, and it is maximum at the Curie temperature of the material [4, 5]. Applications of the MCE at near room-temperature are not restricted to cooling applications [6, 7]; it can also be applied to the development of thermomagnetic motors [8, 9].

For operating temperatures typical of household cooling applications, the MCE is of the order of 2–5 K/T. To amplify this temperature change, heat regeneration is usually employed [5]. Active magnetic regenerators (AMR) are thermal devices in which the magnetocaloric material is packed as a porous matrix subjected to a periodic flow of an aqueous heat transfer fluid. The flow is synchronized with successive magnetization and demagnetization steps of the MCM in the porous bed to produce a refrigerating effect. Thus, the AMR is essentially a cascade of infinitesimal "layers" of MCM that are activated simultaneously to build up a longitudinal temperature profile in the matrix. The layers can be made of the same material, resulting in a homogeneous regenerator. However, given the dependence of the MCE on temperature, it is desirable to build *multilayer* regenerators, where each adjacent layer has a slightly different composition that will function around its own Curie temperature, maximizing the magnetocaloric effect of each portion.

A typical AMR cycle is comprised of the following steps: (1) The magnetic circuit magnetizes the MCM, thereby increasing its temperature due to the MCE; (2) during the *cold blow*, cold fluid previously in thermal contact with the low-temperature source flows through the warm bed, absorbs part of its energy and releases it as heat to the high-temperature sink through the hot heat exchanger; (3) the MCM is demagnetized and cooled down as a result; (4) as the fluid flow is reversed (*hot blow*), it releases energy to the bed, and decreases its temperature so it can absorb the thermal load at the cold heat exchanger in contact with the low-temperature source. Different cycles can be devised by changing the duration and synchronization between the two cycle *characteristic waveforms*:

1. The *applied magnetic field profile*, which describes the oscillating magnetic field over one regenerator;
2. The *fluid flow profile*, which describes the time-variation of flow rate through one bed.

Fluid flow profiles can be more easily investigated experimentally, as no changes in the fluid flow hardware are generally required, provided that a reliable and flexible valving system is in place. In particular, the effect of the *duration* of the fluid blows has been extensively investigated [10–12]. There appears to be a consensus in the literature that the cooling capacity of magnetic refrigerators can be increased by displacing the fluid during periods where the magnetic field is at its extreme values.

Controlling the duration of the fluid blows can be achieved with the use of solenoid valves; a model for a digital hydraulic system and a calculation of valve power has been presented in Refs. [13, 14]. An application of electronic valves in AMR devices has been presented in Ref. [15], using the control logic (for synchronizing the valve operation with the magnetic profile) described in Ref. [16].

In contrast, because of the complexities involved in designing and fabricating magnetic circuits, the applied magnetic field profiles (or simply the magnetic waveforms) are much less studied and are usually investigated in the context of their synchronization with the fluid flow profile using numerical analysis. Considering a trapezoidal magnetic profile and a square fluid flow waveform, one of such analyses showed that small delays between the increase of the magnetic field and the start of the fluid flow are beneficial for the cooling capacity, as they assure that the solid is fully magnetized before initiating its energy transfer with the fluid [17]. To the authors' knowledge, Ref. [18] was the only work to experimentally vary the magnetic profile, by controlling the rotation of magnetic cylinders. They also showed that the cooling capacity of an AMR device depends on the time lag between magnetization and fluid flow.

If the time delay between magnetization and fluid displacement is further increased so that the fluid flow period can coincide with different stages of the magnetic profile, different thermodynamic cycles can be obtained with different performance trends; the Brayton AMR cycle (explained previously) yields the highest cooling capacities, while the Ericsson AMR cycle—with isothermal (de)magnetization steps—yields the highest values of the coefficient of performance [19]. This conclusion was confirmed by a more extensive numerical analysis in Ref. [5], which also varied the amplitude of the trapezoidal magnetic profile and proposed magnetic circuit designs capable of generating such profiles. Reference [20] carried out a numerical comparison of the square wave (step change), sinusoidal and rectified cosine magnetic profiles for a sinusoidal fluid profile and concluded that the cooling capacity and maximum temperature spans are maximal for the instantaneous magnetic profile.

As previously noted, the fluid flow profile is implemented with a proper design of the fluid flow system, while the magnetic profile is an important input when designing a magnetic circuit [21]. With the goal of AMR design in mind, none of the works revised in this paper considered different *shapes* and *amplitudes* of the magnetic field waveform. Regarding shape, the combination of a trapezoidal magnetic profile and an instantaneous fluid flow profile currently prevails in the literature [17, 18, 22], and this is also the situation investigated in the present paper. However, sinusoidal magnetic profiles can be achieved with more compact systems [23], and their generation and impact on AMR performance have been investigated in our group [24, 25]. However, no work has investigated how these waveforms, when synchronized with optimized fluid flow profiles, measure up against the instantaneous magnetic profile, which is recognized in the literature as the optimal waveform for when the fluid flow profile is fixed.

As far as the incorporation of the magnetic field waveform in the AMR performance optimization is concerned, the studies published in the open literature can be classified into three categories, namely *segregated*, *semi-segregated* and *integrated* design. In the first category, the magnetic field waveform remains constant (i.e., fixed shape and amplitude) during the AMR optimization. In the semi-segregated approach, parameters associated with the magnetic field waveform are allowed to change, but no consideration is given to the configuration of the magnetic circuit (i.e., magnet materials, geometry, segmentation) needed to generate such waveforms. Finally, in the integrated design approach, the magnetic circuit that generates the waveform is mathematically incorporated in the analysis (through conservation equations and appropriate closure relationships involving the magnetic field), so objective functions may now be formulated involving the mass, size, geometry or material cost of the magnetic circuit. References [26, 27] are examples of segregated AMR optimization. In Ref. [26], single-objective optimization coupled with a dimensionless parametric analysis enabled identifying the utilization factor that optimized the performance of Gd-based AMRs in terms of the temperature span and cooling capacity. Reference [27] introduced a detailed numerical model of a sixteen-layer La–Fe–Mn–Si–H parallel-plate AMR, and coupled it with a DoE-based (design of experiment) optimization method. A square wave magnetic field waveform with a 1.5-T maximum magnetic flux density was applied. Examples of semi-segregated AMR optimization are given in Refs. [28–30], where multi-objective optimization techniques were employed to optimize the performance of parallel-plate [30] and sphere packed-bed AMRs [29] using methods such as weighted sum, weighted product and genetic algorithms, among others. A common finding to all of such studies is that no configuration exists which can simultaneously optimize all objectives (e.g., cooling capacity and temperature span), so a compromise is required according to specified design constraints. Finally, in their *integrated* approach to AMR optimization, Ref. [31] employed a topology-based optimization of the magnetic circuit (using genetic algorithms) to reduce to a minimum the cost of cooling. In this sense, not only the capital costs were considered (using simple prismatic magnet segments in the magnetic circuit), but also the operating costs associated with the AMR itself. More recently, in Ref. [25], a magnetic circuit consisting of concentric Halbach cylinders was analytically modeled and integrated with models for the power expenditure of the flow management system and for the fluid flow and heat transfer in the AMR to determine the geometric characteristics of the latter which maximized its performance. Designer maps, which embodied the existing trade-offs between the system variables, provided easy visual access to the regenerator dimensions which maximized the cooling capacity or the COP.

The present work complements the previously mentioned studies by investigating the performance of a magnetic refrigerator subjected to different magnetic profile waveforms. The cooling capacity and the COP are calculated taking account of the magnetic profile parameters, while also considering how the AMR geometry affects the performance parameters in conjunction with the magnetic profile. To simplify the analysis, the shape of the fluid flow waveform is assumed fixed, but some of its parameters are also varied. To emulate constraints on an operating point of actual magnetic refrigeration devices, the temperature span is kept fixed, so a few comments are made regarding the second-law efficiency.

2 Materials and methods

As explained before, we performed numerical simulations using a previously developed AMR model, varying the profile-specific and geometric parameters. We also implemented a model to calculate the power consumption of a novel fluid management system, which is a topic not yet extensively studied in the literature. The output variables from this integrated model are the cooling capacity, the several power contributions (the magnetic power to magnetize the material, the pumping power to overcome pressure drop in the regenerator and the power to actuate the electronic valves) and the coefficient of performance (COP).

2.1 AMR model

2.1.1 Governing equations

Simulations were performed using a one-dimensional AMR mathematical model, implemented using the finite volume method [32]. The model solves momentum and energy balance equations for the solid and fluid phases, represented by indices "s" and "f," respectively. The model geometry is shown in Table 1 and assumes that the regenerator is composed of monodisperse packed spheres with porosity ε.

The momentum equation for the fluid domain is given by:

$$\frac{\rho_{\mathrm{f}}}{\varepsilon}\frac{\partial V_z}{\partial t} = -\frac{\partial P}{\partial z} - \frac{\mu_{\mathrm{f}}}{K}V_z - \frac{c_{\mathrm{E}}\rho_{\mathrm{f}}}{K^{1/2}}\left|V_z\right|V_z \tag{1}$$

where the macroscopic inertial term on the left-hand side is balanced with the pressure gradient, Darcy stress and Forchheimer drag [33]. The momentum equation is solved for the time-dependent uniform fluid velocity V_z through the bed.

The energy equation for the fluid phase can be written as:

$$\begin{aligned}\rho_{\mathrm{f}}c_{p,\mathrm{f}}\left(\varepsilon\frac{\partial T_{\mathrm{f}}}{\partial t} + V_z\frac{\partial T_{\mathrm{f}}}{\partial z}\right) = &-\hbar_{\mathrm{sf}}\beta\left(T_{\mathrm{f}} - T_{\mathrm{s}}\right)\\ &+\left|V_z\frac{\partial P}{\partial z}\bigg|_f\right|\\ &+\varepsilon\left(k_{\mathrm{f}}^{\mathrm{eff}} + \rho_{\mathrm{f}}c_{p,\mathrm{f}}D_{\mathrm{ld}}\right)\frac{\partial^2 T_{\mathrm{f}}}{\partial z^2}\\ &+\dot{q}_{\mathrm{csg}}\end{aligned} \tag{2}$$

where the left-hand side includes the inertial and advection terms, and the right-hand side includes terms for the

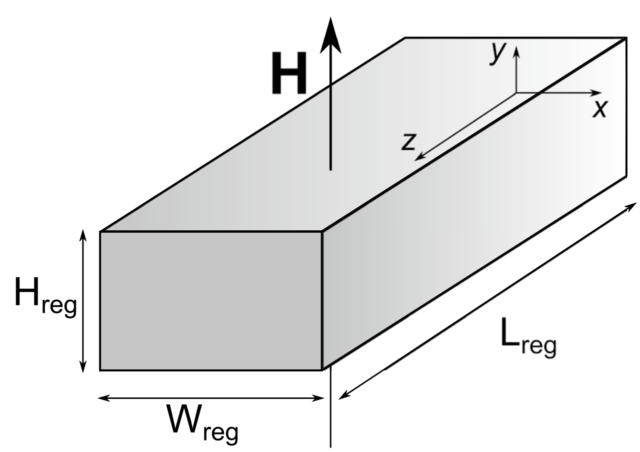

Fig. 1 AMR model geometry

solid-fluid heat transfer, viscous dissipation, heat conduction, porous-media dispersion and casing losses.

The energy equation for the solid phase is written as:

$$\rho_s c_s (1-\varepsilon)\frac{\partial T_s}{\partial t} = \hbar_{sf}\beta(T_f - T_s) + (1-\varepsilon)k_s^{eff}\frac{\partial^2 T_s}{\partial z^2} \quad (3)$$

where the terms represent, respectively, inertia, solid-fluid heat transfer and heat conduction.

Initial and boundary conditions, closure relations for the porous media terms, solution methods and convergence criteria and analyses are discussed in detail in [32]. This AMR model solves the above equations for one regenerator operating between given source temperatures (assuming ideal heat exchangers in contact with the thermal reservoirs), during one full cycle (hot and cold blows and magnetization and demagnetization periods), given specified operating conditions (to be discussed later).

The casing heat transfer term $\dot{q}_{csg}$ in Eq. 2 is calculated solving the heat conduction equation in the regenerator casing [32]. It can be neglected in some circumstances if an insulating casing material is assumed, which greatly simplifies the analysis.

2.1.2 Fluid flow profile modeling

The pressure gradient in Eq. 1 is modeled as:

$$-\frac{\partial P}{\partial z} = \rho_f A_t g(t) \quad (4)$$

where $g(t)$ is a dimensionless function that expresses the mathematical waveform of the pressure gradient, and A_t is its amplitude, adjusted in a convergence loop. In this loop, the mass flow rate calculated in terms of the Darcy velocity from Eq. 1 is compared with the input mass flow rate until convergence is obtained.

The canonical fluid flow profile considered in this work is the square wave or *instantaneous profile*, because of the instantaneous change in flow rate, as shown in Fig. 2.

The instantaneous mass flow rate, $\dot{m}_f(t)$, is defined over a cycle with a period τ, and represents the fluid flow through a given regenerator bed. The so-called *hot cycle*, during which the MCM is magnetized, occupies the time interval $0 \le t < \tau/2$, while the *cold cycle* lies between $\tau/2 \le t \le \tau$. The flow profile oscillates between two plateaus of equal magnitude $\dot{m}_{f,max}$ and opposite directions, which are centered in each half-cycle. During the hot cycle, the cold blow period is τ_{CB}, and during the cold cycle the hot blow period is τ_{HB}. If balanced flow exists, then $\tau_{CB} = \tau_{HB}$.

During each half-cycle, there are periods without fluid flow defined as:

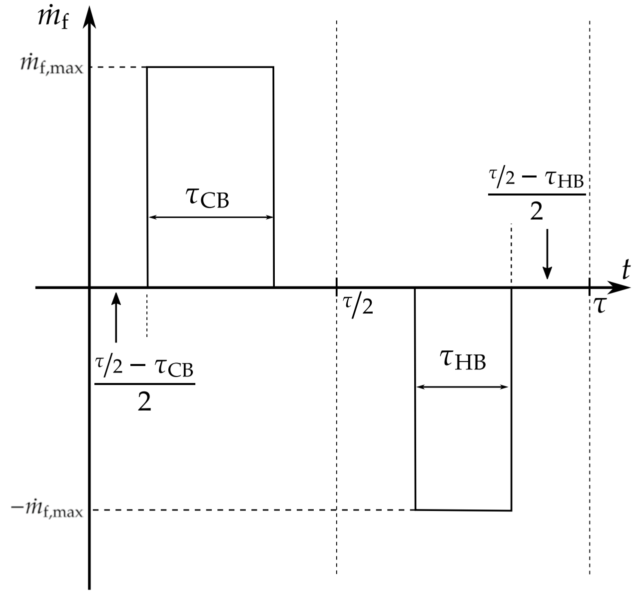

Fig. 2 Instantaneous fluid flow profile. Adapted from [25]

$$\tau_{0,HC} = \frac{\tau/2 - \tau_{CB}}{2} \quad (5)$$

$$\tau_{0,CC} = \frac{\tau/2 - \tau_{HB}}{2} \quad (6)$$

where HC and CC stand for hot cycle and cold cycle, respectively.

The fluid flow profile can be mathematically defined as:

$$\dot{m}_f(t) = \begin{cases} 0, & 0 \le t < \tau_{0,HC} \\ \dot{m}_{f,max}, & \tau_{0,HC} \le t \le \tau/2 - \tau_{0,HC} \\ 0, & \tau/2 - \tau_{0,HC} < t < \tau/2 + \tau_{0,CC} \\ -\dot{m}_{f,max}, & \tau/2 + \tau_{0,CC} \le t \le \tau - \tau_{0,CC} \\ 0, & \tau - \tau_{0,CC} < t < \tau \end{cases} \quad (7)$$

When the blows have different time durations, the AMR cycle is considered unbalanced, and that is known to have a negative effect on performance [11, 34]. In this work, the blows are always balanced; hence, the blow fraction, i.e., the ratio of blow durations to cycle period [11], can be evaluated as:

$$F_B = \frac{2\tau_B}{\tau} \quad (8)$$

where τ_B is the duration of one blow.

2.1.3 Magnetic profile modeling

The magnetic profile is modeled by a waveform of magnetic field strength, $H(t)$, applied perpendicular to the regenerators, as shown in Fig. 1. The magnetic field is assumed uniform throughout the beds. The applied field is corrected from demagnetization effects to yield the effective field inside the regenerators:

$$H^{\mathrm{eff}} = H - N_{\mathrm{D}}M \tag{9}$$

where M is the magnetization field of the material, and N_{D} is a demagnetization factor.

The magnetocaloric effect is implemented using the so-called discrete approach [35]; every time the magnetic field changes, based on the input magnetic profile, the solid temperature is calculated according to:

$$T_{\mathrm{s}}(t + \Delta t) = T_{\mathrm{s}}(t) + \Delta T_{\mathrm{ad}}\left(T_{\mathrm{s}}(t), H^{\mathrm{eff}}(t), H^{\mathrm{eff}}(t + \Delta t)\right) \tag{10}$$

where the adiabatic temperature variation, ΔT_{ad}, a standard measure of the MCE, is calculated from tabulated experimental data for magnetocaloric materials as function of temperature and effective field [32]. Experimental curves for ΔT_{ad} as a function of temperature and magnetic field change can be found in Ref. [36].

The magnetic profiles considered in this work are presented in terms of the flux density $B = \mu_0 H$, where μ_0 is the permeability of free space; the magnetic field H is used in the evaluation of the magnetocaloric effect.

The instantaneous (square wave) profile (represented by the subscript "IT") and the rectified cosine profile (represented by "RC") are defined solely in terms of the extreme values B_{min} and B_{min}, and are shown in Fig. 3.

$$B_{\mathrm{IT}}(t) = \begin{cases} B_{\mathrm{max}}, & 0 \le t < \tau/2 \\ B_{\mathrm{min}}, & \tau/2 \le t < \tau \end{cases} \tag{11}$$

$$B_{\mathrm{RC}}(t) = B_{\mathrm{min}} + \left(B_{\mathrm{max}} - B_{\mathrm{min}}\right)\left|\cos\left(\frac{\pi}{\tau}\left(t - \frac{\tau}{4}\right)\right)\right| \tag{12}$$

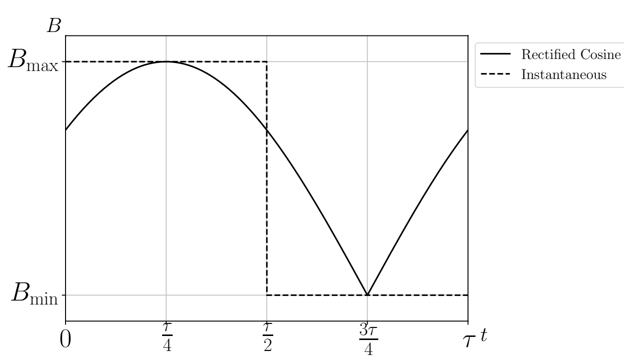

Fig. 3 Instantaneous ("IT") and rectified cosine ("RC") magnetic profiles

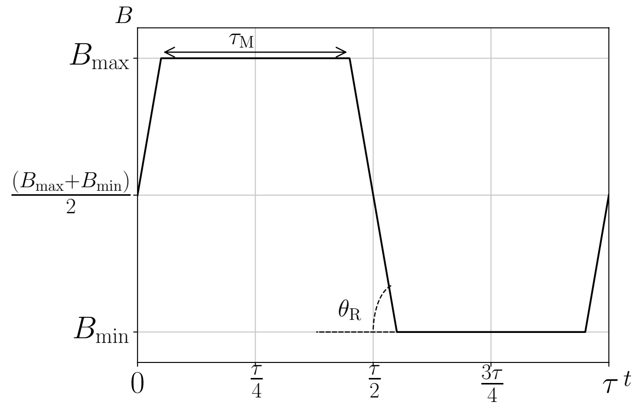

Fig. 4 Magnetic ramp profile

A suitable approximation of the instantaneous profile is the *magnetic ramp profile*, shown in Fig. 4, with finite transition times between the levels of constant magnetization. The magnetic profile oscillates between a low value B_{min} and a high value B_{max}, and remains at each plateau for a period of τ_{M}. The plateaus are balanced and centered at each half-cycle.

The *ramp period* τ_{R} is defined as:

$$\tau_{\mathrm{R}} = \frac{1}{4}\left(\tau - 2\tau_{\mathrm{M}}\right) \tag{13}$$

such that there are four ramp periods in one full cycle. The ramp rate, $\tan\theta_{\mathrm{R}}$, is given by:

$$\tan\theta_{\mathrm{R}} = \frac{\left(B_{\mathrm{max}} - B_{\mathrm{min}}\right)}{2\tau_{\mathrm{R}}} \tag{14}$$

The magnetization fraction, F_{M}, is the fraction of the cycle during which the magnetocaloric material is subjected to a constant magnetic field:

$$F_{\mathrm{M}} = \frac{2\tau_{\mathrm{M}}}{\tau} \tag{15}$$

The ramp profile ("RM") can be mathematically defined as:

$$B_{\mathrm{RM}}(t) = \begin{cases} (B_{\mathrm{max}}+B_{\mathrm{min}})/2 + t\tan\theta_{\mathrm{R}}, & 0 \le t < \tau_{\mathrm{R}} \\ B_{\mathrm{max}}, & \tau_{\mathrm{R}} \le t < \tau/2 - \tau_{\mathrm{R}} \\ B_{\mathrm{max}} - \left(t - \left(\tau/2 - \tau_{\mathrm{R}}\right)\right)\tan\theta_{\mathrm{R}}, & \tau/2 - \tau_{\mathrm{R}} \le t < \tau/2 + \tau_{\mathrm{R}} \\ B_{\mathrm{min}}, & \tau/2 + \tau_{\mathrm{R}} \le t < \tau - \tau_{\mathrm{R}} \\ B_{\mathrm{min}} + \left(t - \left(\tau - \tau_{\mathrm{R}}\right)\right)\tan\theta_{\mathrm{R}}, & \tau - \tau_{\mathrm{R}} \le t \le \tau \end{cases} \tag{16}$$

Additionally, the average values of the magnetic field during each half-AMR cycle are considered for comparison between profiles. The average magnetic profile during the hot cycle ($0 \le t < \tau/2$) is denoted by $\overline{B}_{\mathrm{high}}$ and the average during the cold cycle ($\tau/2 \le t < \tau$) is denoted by $\overline{B}_{\mathrm{low}}$. For the instantaneous waveform, these average values are identical to the extreme values.

2.1.4 Evaluation of solid and fluid properties

The fluid properties are considered constant in the momentum equation to decouple the solution procedures to determine the velocity and temperature fields. The properties are computed at the average temperature between the hot and cold sources, and are evaluated from interpolation of tables imported from the EES software [37]. In all simulations shown in this work, the heat transfer fluid is a 80/20 vol% mixture of water/ethylene glycol. For the energy equations, the fluid properties are also calculated from tabulated data, but the temperature dependence is considered.

Both single- and multilayer regenerators are considered in this study. Single-layer regenerators are composed of gadolinium (Gd), a benchmark material with a Curie temperature of 290 K. For simplicity, the solid density is assumed constant at $\rho_s = 7900\,\mathrm{kg/m^3}$ and the solid thermal conductivity is set to $k_s = 10.5\mathrm{W/(mK)}$. The specific heat capacity of Gd is calculated as a function of temperature and magnetic field based on experimental data, using a bilinear interpolation scheme; more details on the experimental dataset are available in [32].

For the multilayer simulations, gadolinium-yttrium alloys are used, $Gd_{1-x}Y_x$, where x is the yttrium fraction. This fraction reduces the Curie temperature of the alloy relative to that of pure gadolinium. Due to the lack of experimental data on the magnetocaloric properties of $Gd_{1-x}Y_x$ alloys at the time this analysis was made, a simpler approach was used in which the dependence of magnetization, specific heat capacity and entropy with respect to the magnetic field for alloys with a low yttrium fraction are identical to those of pure gadolinium, but are shifted to a lower Curie temperature (corresponding to the yttrium fraction).

2.1.5 Performance metrics

The AMR model is solved for only one bed, but assumes that the N_{reg} identical beds experience the same cycle. Thus, the extensive performance parameters are multiplied by that factor. The cooling capacity is calculated as [32]:

$$\dot{Q}_C = N_{reg}\frac{1}{\tau}\int_{\tau_{HB}} \dot{m}_f(t)c_{p,f}\left(T_C - T_{f,CE}\right)dt \tag{17}$$

As pointed out in Ref. [25], since external sources of irreversibility (e.g., heat transfer with a finite temperature difference in the heat exchangers) are ignored and no eddy currents and hysteresis losses are present, the magnetic power required to magnetize the solid refrigerant and produce the MCE in the AMR cycle is given by the product of the Carnot efficiency and the cooling capacity as follows:

$$\dot{W}_{mag} = \dot{Q}_C\frac{T_H - T_C}{T_C} \tag{18}$$

Irreversibility due to fluid friction is accounted for in the calculation of the pumping power:

$$\dot{W}_{pump} = N_{reg}\frac{1}{\tau}\int_0^{\tau}\frac{\dot{m}_f}{\rho_f}\Delta P dt \tag{19}$$

where ΔP is the total pressure drop through the regenerator (including one hot and one cold blow).

2.2 Hydraulic system and fluid flow profile model

The hydraulic system designed to modulate the fluid flow through different regenerators at different time instants is composed of a pump and a set of electronic valves which can be precisely controlled to yield the desired blow durations. The electrical power consumed by the valve array is computed separately from other work contributions.

In the present analysis, two types of valves are considered. In the first approach, called *Type R valves*, the model proposed in Ref. [13] is used, assuming that the individual power consumption of each valve is independent of frequency and blow fraction. The valve power, $\dot{W}_{valve}$, can be computed as:

$$\dot{W}_{valve} = N_{valve}F_B\left(\dot{W}_{valve,n} + \frac{1}{2}\dot{W}_{relay,n}\right) \tag{20}$$

where N_{valve} is the number of valves, $\dot{W}_{valve,n}$ is the measured average nominal power for one normally closed electronic valve and $\dot{W}_{relay,n}$ is the nominal power for one controlling relay. The factor $\frac{1}{2}$ is due to two valves being controlled by one relay.

In the second approach, *Type S valves* are used, which have a nominal power lower in magnitude, but which depends on the frequency and blow fraction. These valves were experimentally characterized in Ref. [14], where a single valve was attached to a measurement circuit and set to operate for a range of values of blow fraction and frequency; the valve power was calculated from the averaged values of voltage and current after the periodic steady state was reached. From those experiments, the valve power was experimentally correlated as:

$$\dot{W}_{valve}\,[\mathrm{W}] = N_{valve}\left(0.927f\,[\mathrm{Hz}] + 1.023F_B + 0.226f\,[\mathrm{Hz}]F_B - 0.037\right) \tag{21}$$

Equation (21) was correlated for blow fractions of 50 and 100 % and frequencies in the range of 0.2–1.6 Hz, with an uncertainty on the order of 0.4 W for a single valve. The use of different valve types will be discussed in the Results section.

Independent of the valve type used, it is also assumed that each valve system is capable of producing the fluid flow profile shown in Fig. 2, where the displaced fluid mass during one blow in one regenerator bed is $\dot{m}_{\mathrm{f,max}} F_{\mathrm{B}} \tau/2$. The *utilization factor* can then be calculated as:

$$\Phi = \frac{\dot{m}_{\mathrm{f,max}} F_{\mathrm{B}} c_{p,\mathrm{f}}}{2 f m_{\mathrm{s}} c_{\mathrm{s}}} \tag{22}$$

and in all results shown in this work, the number of valves is calculated as:

$$N_{\mathrm{valve}} = 2N_{\mathrm{reg}} \tag{23}$$

2.3 Coefficient of performance and second-law efficiency

The coefficient of performance is calculated as the ratio of the cooling capacity—the main output parameter from the AMR model—and all previously cited power contributions:

$$\mathrm{COP} = \frac{\dot{Q}_{\mathrm{C}}}{\dot{W}_{\mathrm{pump}} + \dot{W}_{\mathrm{mag}} + \dot{W}_{\mathrm{valve}}} \tag{24}$$

The maximum possible COP between the source temperatures is the Carnot COP, calculated as:

$$\mathrm{COP}_{\mathrm{Carnot}} = \frac{T_{\mathrm{C}}}{T_{\mathrm{H}} - T_{\mathrm{C}}} \tag{25}$$

and the second-law efficiency is defined as:

$$\eta_{\mathrm{2nd}} = \frac{\mathrm{COP}}{\mathrm{COP}_{\mathrm{Carnot}}} \tag{26}$$

3 Results and discussions

The analysis of the magnetic profiles was performed at two different stages. Initially, the instantaneous (square-wave) and the rectified cosine profiles are compared using a simpler approach (i.e., neglecting casing losses). Later, based on the selection of the most promising magnetic profile, a more in-depth analysis was carried out to determine the optimal geometric and operating parameters of the AMR system.

3.1 Comparison of instantaneous and rectified cosine profiles using a simplified model

At the first stage of the present analysis, the instantaneous and rectified cosine profiles are compared considering a single-layer regenerator without casing losses, using Type R valves. The parameters used in all simulations are presented in Table 1.

Table 1 AMR parameters kept fixed in the simulations with different magnetic profiles

Parameter	Value
D_{p}	0.5 mm
H_{reg}	20 mm
W_{reg}	25 mm
L_{reg}	100 mm
N_{reg}	11
N_{valve}	22
T_{H}	298 K
T_{C}	278 K
$\dot{W}_{\mathrm{valve,n}}$	4 W
$\dot{W}_{\mathrm{relay,n}}$	0.36 W

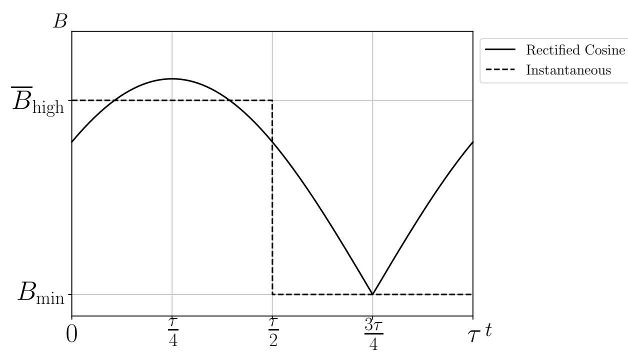

Fig. 5 Configuration of average and extreme values of the instantaneous and rectified cosine profiles

When comparing the performances resulting from the application of the different magnetic profiles, the same average magnetic field during the hot cycle will be considered; this implies a higher peak for the rectified cosine. For the cold cycle, the minimum values for both profiles are the same, as shown in Fig. 5. As a reference, in all simulations, the minimum value for the rectified cosine was fixed at $B_{\mathrm{min}} = 0.1$ T.

Simulations were carried out for various values of blow fraction. The rectified cosine profile can benefit from smaller blow fractions that concentrate the flow during the periods of very high and very low fields, thereby increasing the average variation in magnetic field [11]; this is not observed with the instantaneous profile, since the field is constant and reducing the blow fraction will only reduce the period when the fluid is in contact with the warm solid, decreasing the regenerator effectiveness. In this section, all results use the critical value of blow fraction that maximized the cooling capacity: fluid flowing during the entire period for the instantaneous profile, and only during 60

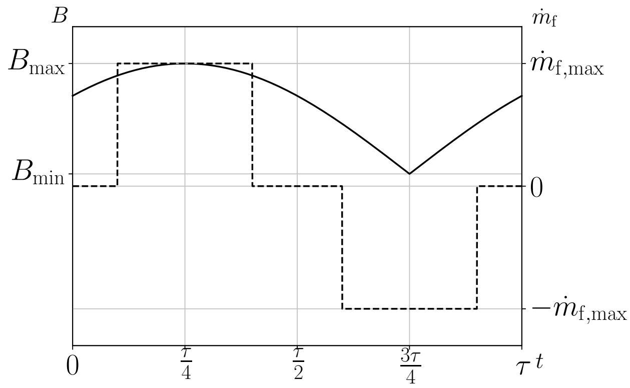

Fig. 6 Rectified cosine magnetic profile (solid lines) and the instantaneous flow profile with blow fraction of 60 % (dashed lines)

% of the period (the smallest blow fraction tested) for the cosine profile; this latter case is shown in Fig. 6.

Figure 7 shows the cooling capacity attained by the device at a frequency of 1 Hz for different utilizations. The horizontal axis shows the average field value during the high field region. The instantaneous profile almost always yields a higher performance, and since the average field during the hot cycle (high field stage) is the same, the main difference is due to the low magnetic field levels. In this comparison, the instantaneous profile is capable of keeping a low magnetic field over the entire half-cycle, which is beneficial for performance; as demonstrated in Ref. [20], a higher average magnetic field during the low-field stage increases the solid temperature and consequently results in warmer fluid entering the cold heat exchanger, representing a thermal loss. Analyzing points of different profiles of constant utilization (which should result in the same regenerator effectiveness), for $\Phi = 1.0$ and $B_{high} = 1.40$T, the cooling capacity for the instantaneous profile is 196.3 % higher than for the cosine profile. This results from the fluid being able to cool down to lower temperatures during the low-field cycle, since the cosine profile cannot maintain the field as low as the instantaneous profile (cf. Fig. 5), even with the reduction of blow fraction.

The only exception in this comparison is observed for the lowest utilization of $\Phi = 0.2$, where the performance is slightly better for the RC profile. Since the blow fraction for the cosine is smaller, the mass flow rate is higher in the latter for the same utilization [cf. Eq. (12)]. This increases the heat transfer rate, as previously explained—outweighing the effects of the magnetic field.

Also noticeable in Fig. 7 is the nonlinear relationship between cooling capacity and utilization. For instance, for the "RC" profile at the highest magnetic field, the cooling capacity increases when the utilization is raised from 0.2 to 0.6, but then returns to the same levels with a further increase of the utilization to 1.0. Since the frequency is constant in Fig. 7, increasing the utilization means increasing the mass flow rate; initially, this results in higher heat transfer rates due to higher Nusselt numbers, but further increase reduces the effectiveness and amplifies viscous dissipation, to the point where the cooling capacity is null for certain points with the highest utilization.

The same analysis, but in terms of the coefficient of performance, is shown in Fig. 8, where the instantaneous profile yields better results for medium to high levels of utilization. This can be explained based on the behavior of the magnetic, valve and pumping powers shown in Fig. 9 for a fixed utilization of 0.6. As can be seen, the magnetic power only differs between the profiles due to changes in cooling capacity. Also, the valve power is higher for the instantaneous

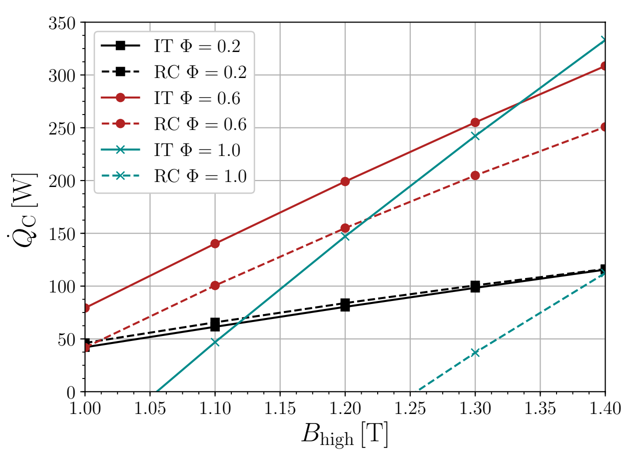

Fig. 7 Cooling capacity as a function of the average high magnetic field, for different utilizations. "IT": instantaneous (blow fraction of 100 %); "RC": rectified cosine (blow fraction of 60 %)

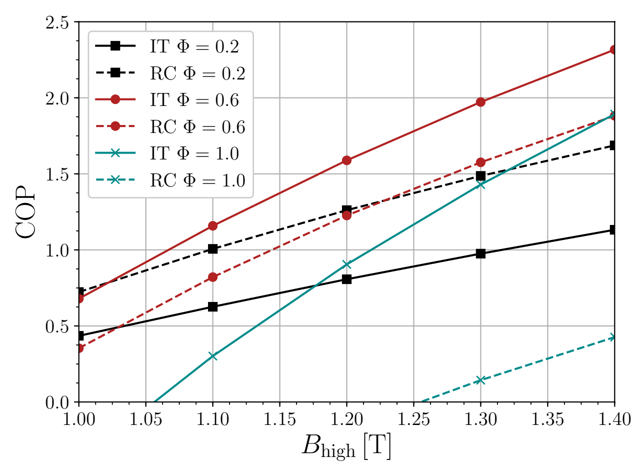

Fig. 8 Coefficient of performance as a function of the average high magnetic field, for different values of utilization. "IT": instantaneous (blow fraction of 100 %); "RC": rectified cosine (blow fraction of 60 %)

Fig. 9 Power contributions as a function of the average high magnetic field, for a utilization of 0.6. "IT": instantaneous (blow fraction of 100 %); "RC": rectified cosine (blow fraction of 60 %)

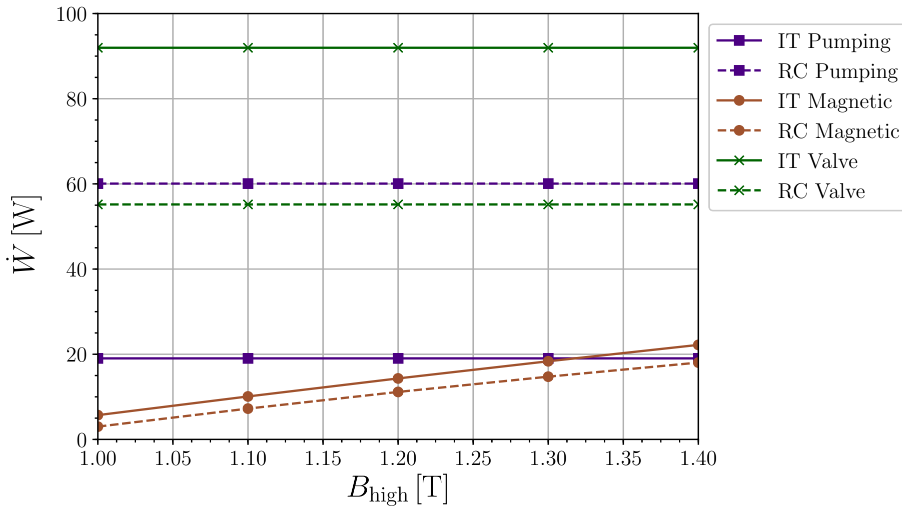

profile since the valves must remain open for longer periods. However, the proportional increase in pumping power, due to larger flow rates when operating with the smaller blow fraction of the "RC" profile, is even higher (than the change in valve power). Although not shown in Fig. 9, the effect of higher utilization levels is to make the pumping power even more relevant; as depicted in Fig. 8, the lowest levels of the coefficient of performance are attained with the smallest blow fraction (for the rectified cosine profile) and higher utilization, corresponding to the highest flow rate levels.

In general, considering target values for the cooling capacity, AMRs operating with the instantaneous magnetic profile lead to better performance results. As can be seen in Fig. 7, an instantaneous profile with the lowest possible value of B_{min} and the highest possible value of B_{max}, with a flow profile occupying the whole cycle with average values of utilization, results in the highest values of cooling capacity among all simulations.

The rectified cosine profile, found in compact systems using Halbach arrays, can surely benefit from reducing the blow fraction, both in terms of cooling capacity and temperature span. However, for the typical parameters evaluated in this paper, even if the blow fraction is optimized for the "RC" profile, the "IT" profile still gives better results.

3.1.1 Analysis of the instantaneous profile

As shown in the previous section, the instantaneous profile generally yields the highest values of cooling capacity. Therefore, in this section, a more detailed analysis of this profile is carried out, where the maximum field is varied, but the minimum value is kept at 0.05 T. Figure 10 shows the cooling capacity as a function of the utilization, for several levels of the maximum magnetic field and two different operating frequencies. Because of the conflict between a low heat transfer rate for flow rates that are too low and losses in regenerator effectiveness in flow rates that are too high, there are critical values of utilization that maximize the cooling capacity, and these critical values increase with the magnetic field. For higher magnetic fields, the increase in the MCE surpasses the loss of effectiveness, and one can go to higher flow rates without losing performance. It can also be seen in Fig. 10 that at higher frequencies the values of cooling capacity are higher, and also the critical values of utilization are lower. However, this is usually achieved at the expense of an even higher power consumption at higher frequencies [38, 39], resulting in a decrease of the coefficient of performance with frequency. Critical values of utilization that maximize the COP (all other parameters fixed) are also observed, but these tend to be smaller than the critical values for cooling capacity; at higher utilization levels, the pumping power increases more rapidly than the cooling capacity.

The geometric parameters in Table 1 were chosen from preliminary simulations, so they are not optimal. To understand the impact of the regenerator geometry on the system performance with the instantaneous profile, the regenerator height was varied in Fig. 11, and all other parameters from Table 1 were kept fixed and with $\Phi = 0.4$. The height was chosen as the geometric parameter to be varied as it usually represents a design trade-off in magnetic refrigerators [25]: taller regenerator cross sections allow for more magnetocaloric material while reducing the volume of the magnetic circuit (cf. Fig. 12).

As expected, higher magnetic fields allow for smaller regenerators (hence more compact systems) to achieve a desired cooling capacity. For instance, to achieve a capacity of 100 W, increasing the field from 1.0 to 1.2 T results in regenerators that are 36 % smaller. Comparing the results for the cooling capacity and coefficient of performance, the trends are largely the same, as the former is more sensitive to variations in the magnetic field and regenerator height than the components of power; note that increasing the

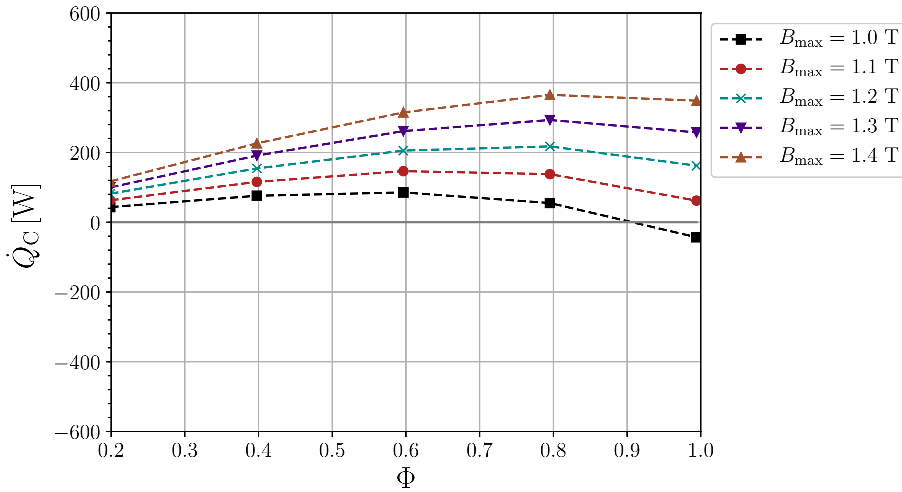

(a) $f = 1$ Hz

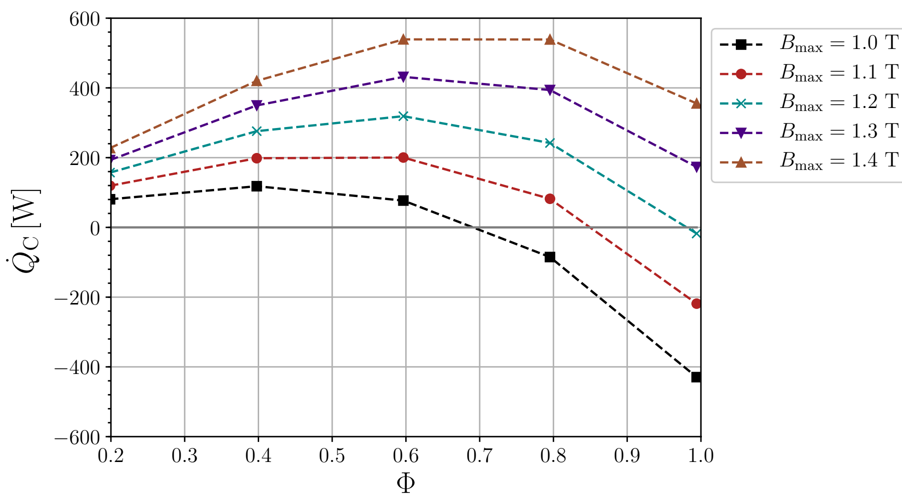

(b) $f = 2$ Hz

Fig. 10 Cooling capacity as a function of utilization, for various values of the high magnetic field for the instantaneous profile

regenerator height increases the mass of magnetocaloric material, hence increasing the cooling capacity, but it also changes the area available for the fluid flow (influencing pumping power) and the demagnetization factor (influencing the magnetic power).

3.2 In-depth analysis of the magnetic ramp profile

Based on the better performance of the instantaneous profile, the ramp profile is a naturally suitable target profile for the design of magnetic refrigerators and will be analyzed in this section, representing the second stage in the analysis of magnetic profiles.

Moving towards a more realistic model, casing losses are included, using the model from Ref. [32]. The bed is enclosed in a solid casing of thickness h_{csg}, and two air layers of thickness h_{air} separate the AMR and its casing from the inner and outer magnet cylinders, as shown in Fig. 12. The optimal design of such magnetic cylinders aiming at a particular magnetic profile will be the subject of future publications.

Preliminary analyses carried out in Ref. [40] showed that a stainless steel casing with a thickness of $h_{csg} = 0.5$ mm is thick enough to ensure mechanical integrity and easy manufacturing, while being thin enough to accommodate the material with a low thermal conductivity.

In addition, in the present study, an air gap clearance thickness was set at $h_{air} = 1$mm. This value gave rise to a peak in cooling capacity due to the compromise between minimizing losses and maximizing the magnetocaloric

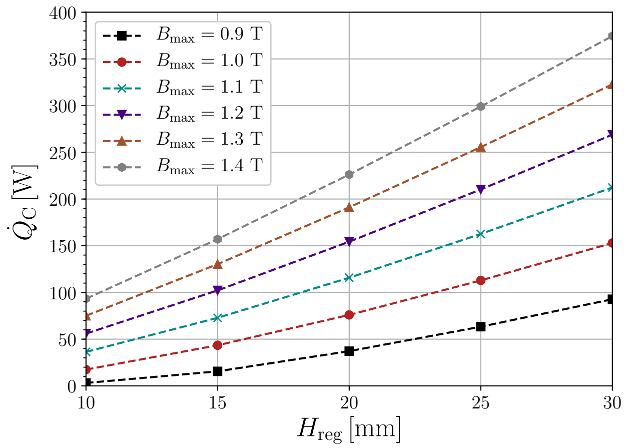

(a) Cooling capacity

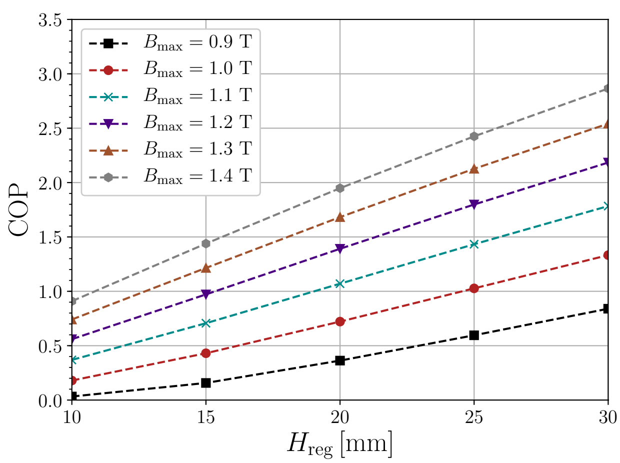

(b) Coefficient of performance

Fig. 11 Performance metrics as a function of the regenerator height (all other parameters were set as in Table 1, for utilization factor of 0.4) for various values of the high magnetic field of the instantaneous profile

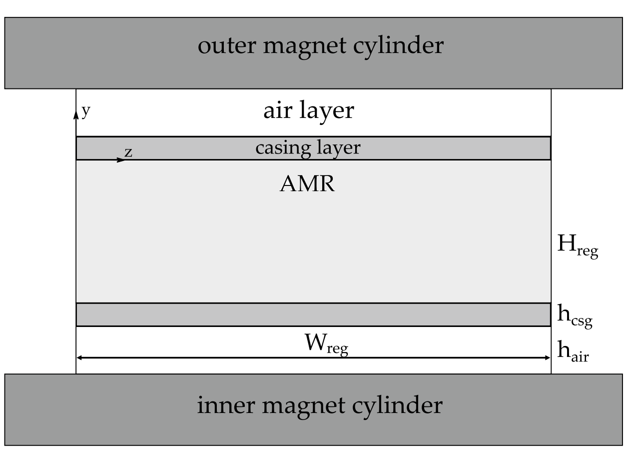

Fig. 12 Model for the casing losses in regenerators

Table 2 Fixed parameters for the AMR simulations used in this chapter

Parameter	Value
W_{reg}	30 mm
L_{reg}	85 mm
N_{reg}	8
N_{valve}	16
f	1 Hz
T_H	305.5 K = 32.5°C
T_C	270.5 K = −2.5°C
D_p	350 µm
h_{csg}	0.5 mm
h_{air}	1 mm
Casing material	Stainless steel
Number of layers	3
Curie temperatures of each layer	273, 283, 290 K
Length fractions of each layer	20, 20, 60 %

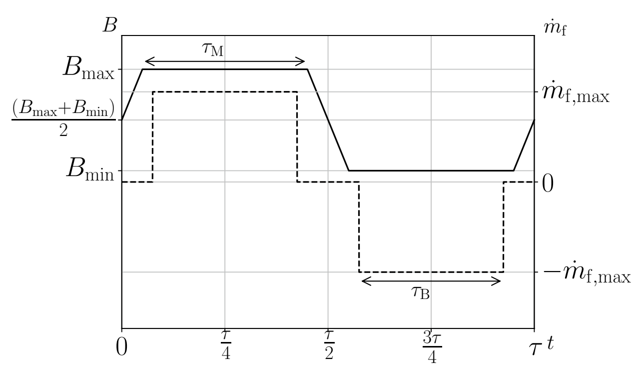

Fig. 13 Comparison between the magnetic ramp profile (solid line) and the instantaneous fluid flow profile (dashed line)

mass. The thermophysical properties of stainless steel and air were also obtained with interpolation of tables exported by the EES software [37].

The simulations in this section also use multilayer regenerators. A summary of all parameters adopted in this section, including the Curie temperatures and volumetric fractions (relative to the length of the bed) of each layer, is presented in Table 2; more details on the selection of these parameters are shown in Ref. [41]. In addition, in the following results, Type S valves are used, with valve power calculated by Eq. 21.

Figure 13 shows the two profiles that will be used in this section and how they are synchronized. Regarding the magnetic profile, the magnitude of the high value will be varied to investigate the performance of the AMR system, while the minimum will be kept fixed at B_{min} = 0.05T.

3.2.1 Performance curves for variable blow and magnetization fractions

Figure 14 shows the cooling capacity and coefficient of performance of the AMR system for a fixed utilization factor of 0.4 and for a magnetic profile with a maximum at 1.3 T, for variable blow and magnetization fractions. To facilitate the analysis, the results are plotted in terms of the ratio F_M/F_B, with curves for different values of F_B. It is clear that both the cooling capacity and the coefficient of performance exhibit a peak at $F_M = F_B$. Moreover, to the right of the peak, i.e., for higher values of F_M, the reduction of both performance metrics is slower, meaning it is better to have a magnetization plateau that is wider than the fluid flow plateau.

The reduction in performance for $F_M > F_B$ can be explained by an increase in heat leakage through the casing, as the solid begins to lose energy to the environment when the fluid is not flowing. For $F_M < F_B$, the fluid begins to flow when the solid is not totally warmed up, losing effectiveness, and this effect is amplified with larger blow fraction values; notice that, to the left of the peak, the performance parameters are the lowest for the highest value of F_B.

The influence of the utilization is demonstrated in Fig. 15, where the cooling capacity is plotted for different utilization factors. For increasing Φ in this range, not only do the

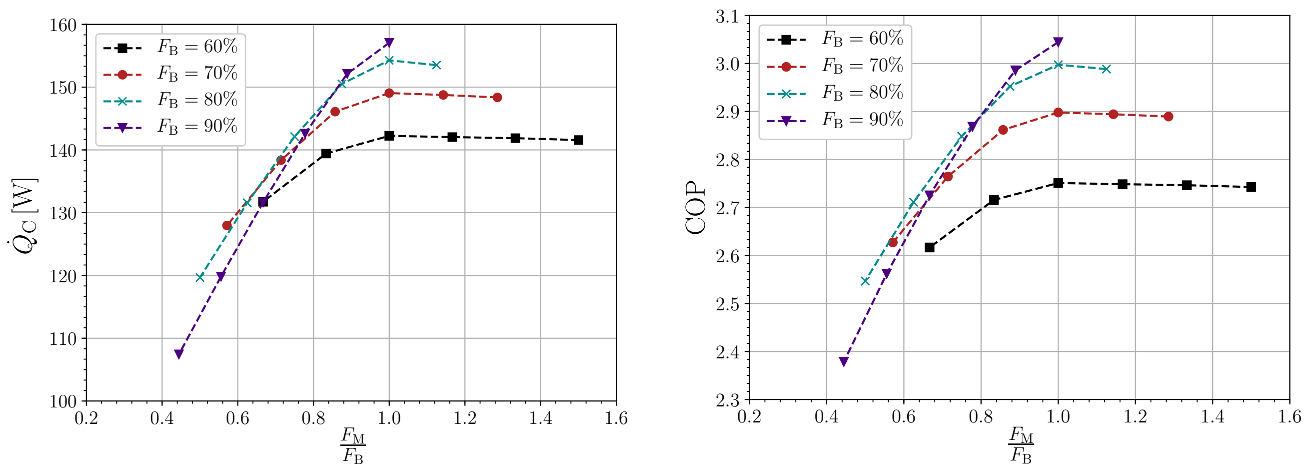

(a) Cooling capacity

(b) Coefficient of performance

Fig. 14 Performance of the AMR system for various blow and magnetization fractions, utilization of 0.4 and high magnetic field of 1.3 T

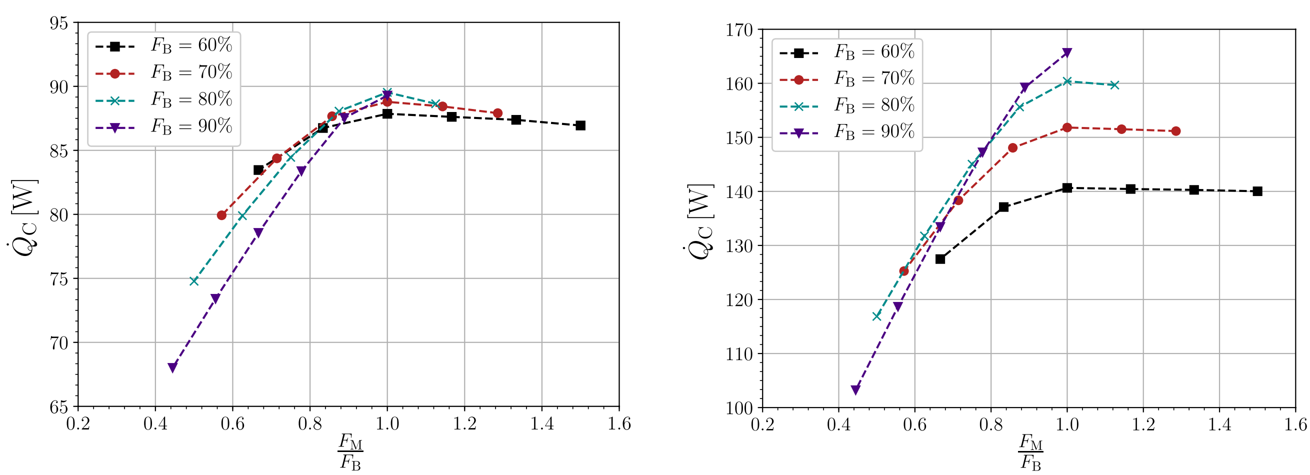

(a) $\Phi = 0.2$

(b) $\Phi = 0.5$

Fig. 15 Influence of utilization on the cooling capacity of the AMR system for various blow and magnetization fractions, with high magnetic field of 1.3 T overall values of cooling capacity increase, but also the importance of choosing the blow fraction becomes clearer. In these ranges of utilization and blow fraction, the cooling capacity increases because the higher transfer rate associated with higher flow rates dominates over the loss of regenerator effectiveness.

The above results can be evaluated from another point of view with Fig. 16, where the coefficient of performance is plotted as contour levels. This type of map is useful because, since B_{min} and τ are fixed, each point in this graph completely characterizes a magnetic ramp profile, and each subplot with fixed Φ and F_{B} characterizes the fluid flow profile. As expected, the performance increases for the higher values both B_{max} and F_{M}, where the magnetic ramp profile tends to the instantaneous magnetic profile with a large amplitude. Confirming the previous trends, the results are less sensitive to the magnetization fraction when $F_{\mathrm{M}} \geq F_{\mathrm{B}}$.

3.2.2 Geometric analysis of the regenerators using the magnetic ramp profile

All previous results assumed a fixed regenerator geometry, with the goal of identifying the optimal fluid and magnetic profile parameters. It became clear that the magnetization fraction should be as large as possible, but that raises some challenges in realizing abrupt changes in the magnetic field. The value of $F_{\mathrm{M}} = 70\%$ is then chosen as a compromise, with a corresponding $F_{\mathrm{B}} = F_{\mathrm{M}}$. The mean value of the utilization factor of $\Phi = 0.4$ is also chosen as reference in the next results.

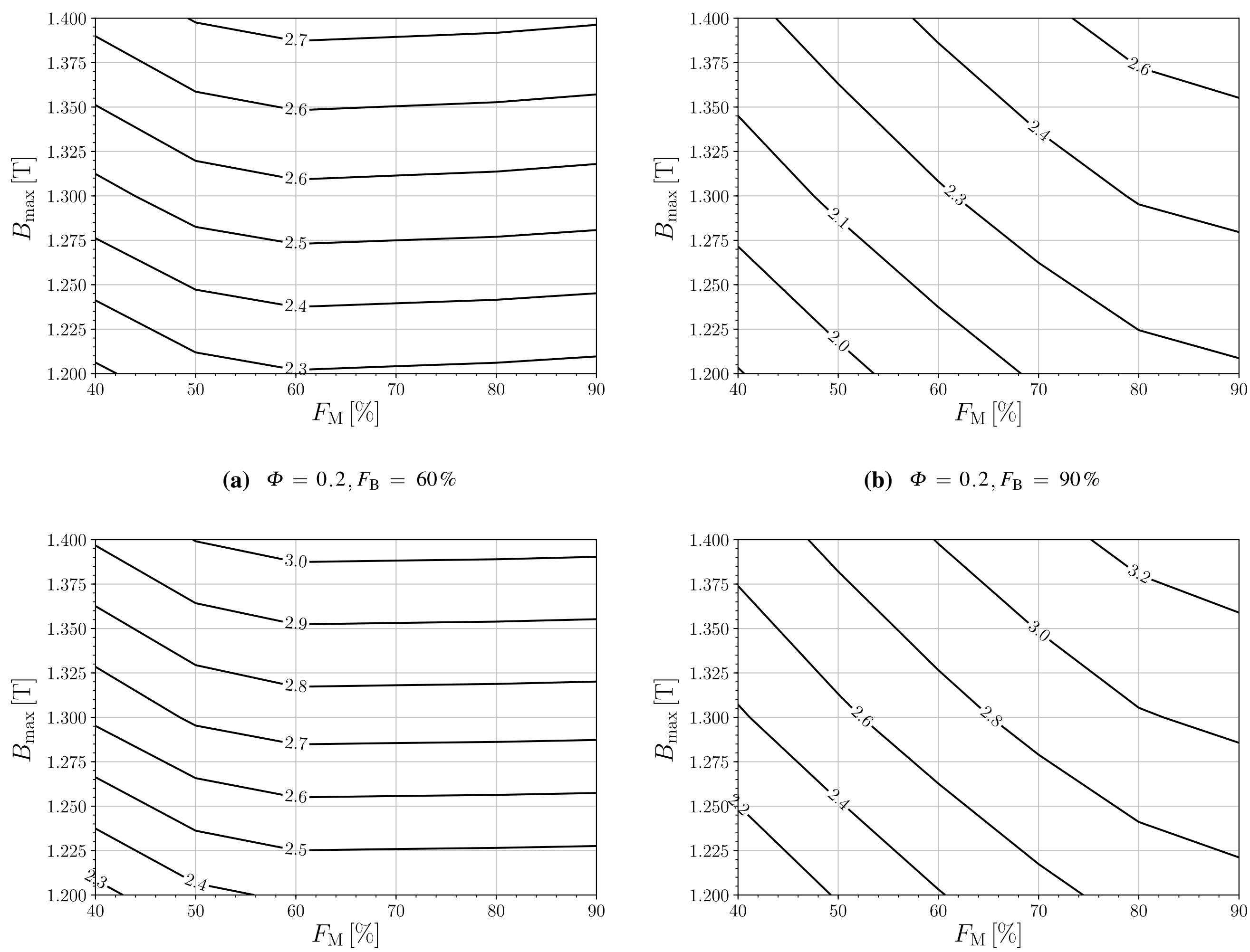

(a) $\Phi = 0.2, F_{\mathrm{B}} = 60\%$ **(b)** $\Phi = 0.2, F_{\mathrm{B}} = 90\%$

(c) $\Phi = 0.4, F_{\mathrm{B}} = 60\%$ **(d)** $\Phi = 0.4, F_{\mathrm{B}} = 90\%$

Fig. 16 Influence of utilization and blow fraction on the coefficient of performance of the AMR system for varying high magnetic field and magnetization fraction

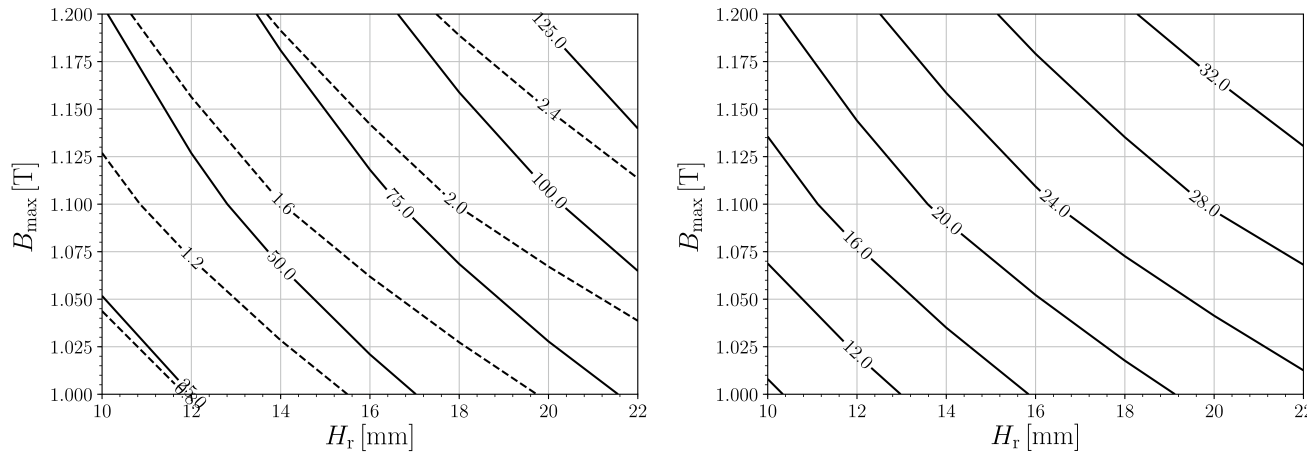

(a) Cooling capacity (solid lines) and coefficient of performance (dashed lines)

(b) Second-law efficiency

Fig. 17 Performance of the AMR with varying regenerator height and high magnetic field, with fixed $F_M = F_B = 70\%$ and $\Phi = 0.4$

Figure 17 shows the cooling capacity, coefficient of performance and second-law efficiency for varying magnetic field and regenerator height. As expected, larger regenerators can produce the desired performance with lower magnetic fields. It can also be seen that this configuration for an AMR system can achieve values of η_{2nd} compatible with conventional vapor compression systems [42, 43], although these numerical results do not include mechanical losses.

4 Conclusions

To the authors' knowledge, this is the first study where magnetic and fluid flow profiles for an AMR model are mathematically modeled and the model parameters are changed in an integrated and systematic way. The instantaneous (square wave), rectified cosine and ramp magnetic profiles were implemented in an AMR model, together with an instantaneous fluid flow profile, and the profile parameters were varied simultaneously with the regenerator geometric parameters. These waveforms can be found in existing MR devices published in the literature. A valve model was also incorporated into a more realistic computation of the coefficient of performance.

When comparing the instantaneous and the rectified cosine magnetic profiles, the cooling capacity associated with the former can be almost 200 % higher than with the latter, for the same utilization and average high magnetic field and considering optimal blow fractions. The rectified cosine profile suffers from high values of the low magnetic field, and a reduction of the blow fraction up to the minimum tested value of 60 % is not enough to overcome the loss in cooling capacity resulting from this effect.

An analysis of power contributions showed that the cost of the higher cooling capacity for the instantaneous profile is a higher valve power associated with the longer blow duration, dominating the other contributions. However, the coefficient of performance is still higher for the square wave. Hence, even though sinusoidal waveforms can be obtained with more compact systems, step-like variations of high amplitude of the magnetic field are preferred if performance is more critical.

The ramp magnetic profile is a feasible approximation for the instantaneous profile without abrupt changes in the magnetic field plateaus. For an AMR device operating with this profile and the instantaneous fluid flow profile, both cooling capacity and coefficient of performance are maximized if the blow duration is equal to the period of constant magnetic field; if this exact synchronization is not possible, making the magnetization plateau wider than the flow plateau results in a smaller reduction of the performance metrics than in the case where the magnetization plateau is narrower.

With this strategy and using average values of utilization, it is possible to achieve second-law efficiency levels compatible with those of vapor compression systems. Hence, the ramp magnetic profile is identified as a suitable target profile in the design of magnetic circuits for AMR devices.

Acknowledgements This work was funded by the INCT (National Institutes of Science and Technology) Program and Conselho Nacional de Desenvolvimento Científico e Tecnológico (CNPq Grant No. 443696/2014-4; FAPESC Grant No. 2018TR1576). Additional funding was provided by CAPES (Talents for Innovation Program - Grant No. 88887.194773/2018-00) to F. Fortkamp and J. Lozano.

Financial support from EMBRAPII, Embraco (now NIDEC-GA) and CODEMGE is also acknowledged.

Compliance with ethical standards

Conflict of interest statement There is no actual or potential conflict of interest including any financial, personal or other relationships with other people or organizations that could inappropriately influence, or be perceived to influence, the present work.

References

1. Bansal P, Vineyard E, Abdelaziz O (2012) Status of not-in-kind refrigeration technologies for household space conditioning, water heating and food refrigeration. Int J Sustain Built Environ 1:85–101
2. IIR (2017) 36th informatory note on refrigeration technologies: flammable refrigerants. http://www.iifiir.org/userfiles/file/publications/notes/NoteTech_36_EN_nkyix2fcj7.pdf, 2017. Accessed 30 Oct 2018
3. Lionte S, Risser M, Vasile C, Elouad L, Muller C (2018) Adapting an active magnetic regenerator to a continuous fluid flow application. Int J Refrig 85:303–313
4. Smith A, Bahl CRH, Bjørk R, Engelbrecht K, Nielsen KK, Pryds N (2012) Materials challenges for high performance magnetocaloric refrigeration devices. Adv Energy Mater 2:1288–1318
5. Kitanovski A, Plaznik U, Tušek J, Poredoš A (2014) New thermodynamic cycles for magnetic refrigeration. Int J Refrig 37:28–35
6. Gimaev R, Spichkin Y, Kovalev B, Kamilov K, Zverev V, Tishin A (2019) Review on magnetic refrigeration devices based on HTSC materials. Int J Refrig 100:1–12
7. Greco A, Aprea C, Maiorino A, Masselli C (2019) A review of the state of the art of solid-state caloric cooling processes at room-temperature before 2019. Int J Refrig 106:66–88
8. Kitanovski A (2020) Energy applications of magnetocaloric materials. Adv Energy Mater 10:1903741
9. Kaneko GH, Souza AC, Moro F, Colman FC, Conceição WAS, Alves CS, Trevizoli PV (2019) Design and assembling of a magnetic circuit for a thermomagnetic motor apparatus. J Braz Soc Mech Sci Eng 41:394
10. Teyber R, Trevizoli PV, Niknia I, Christiaanse TV, Govindappa P, Rowe A (2017a) Experimental performance investigation of an active magnetic regenerator subject to different fluid flow waveforms. Int J Refrig 74:38–46
11. Nakashima ATD, Dutra SL, Trevizoli PV, Barbosa JR Jr (2018a) Influence of the flow rate waveform and mass imbalance on the performance of active magnetic regenerators. Part I: experimental analysis. Int J Refrig 93:236–248
12. Fortkamp FP, Eriksen D, Engelbrecht K, Bahl CRH, Lozano JA, Barbosa JR Jr (2018) Experimental investigation of different fluid flow profiles in a rotary multi-bed active magnetic regenerator device. Int J Refrig 91:46–54
13. Cardoso PO, Destro MC, Alvarez MG, Lozano JA, Barbosa Jr JR, De Negri VJ (2016) Transient model and energy assessment of a digital solenoid valve system for a magnetic refrigerator. In: Proceedings of the 16th Brazilian congress of thermal sciences and engineering, Vitória, Brazil
14. Cardoso PO (2018) An electrovalve system for hydraulic management of active magnetic regenerators, 2018. Master's thesis (Mechanical Engineering), Federal University of Santa Catarina (in Portuguese)
15. Nakashima ATD, Dutra SL, Hoffmann G, Lozano JA, Barbosa Jr JR (2018) Performance assessment of solenoid valves as flow distributors for an active magnetic regenerator. In *Proceedings of the 8th international conference on caloric cooling (Thermag VIII)*, Darmstadt, Germany
16. Hoffmann G, Dutra SL, Cardoso PO, Nakashima ATD, Lozano JA, Barbosa Jr JR (2017) Actuation and control of electric valves for a magnetic refrigerator. In: Proceedings of the 24th ABCM international congress of mechanical engineering (COBEM 2017), Curitiba, Brazil
17. Bjørk R, Engelbrecht K (2011) The influence of the magnetic field on the performance of an active magnetic regenerator (AMR). Int J Refrig 34:192–203
18. Benedict MA, Sherif SA, Beers DG, Schroeder MG (2016) Design and performance of a novel magnetocaloric heat pump. Sci Technol Built Environ 22(5):520–526
19. Plaznik U, Tušek J, Kitanovski A, Poredoš A (2013) Numerical and experimental analyses of different magnetic thermodynamic cycles with an active magnetic regenerator. Appl Therm Eng 59:52–59
20. Trevizoli PV, Barbosa JR Jr, Tura A, Arnold D, Rowe A (2014) Modeling of thermomagnetic phenomena in active magnetocaloric regenerators. J Therm Sci Eng Appl 6:031016
21. Oh S, Min S, Hong J-P (2013) Air gap flux density waveform design of surface-mounted permanent magnet motor considering magnet shape and magnetization direction. IEEE Trans Magn 49(5):2393–2396
22. Park I, Jeong S (2017) Development of the active magnetic regenerative refrigerator operating between 77 and 20 K with the conduction cooled high temperature superconducting magnet. Cryogenics 88:106–115
23. Trevizoli PV, Christiaanse TV, Govindappa P, Niknia I, Teyber R, Barbosa JR Jr, Rowe A (2016a) Magnetic heat pumps: an overview of design principles and challenges. Sci Technol Built Environ 22(5):507–519
24. Fortkamp FP, Lozano JA, Barbosa JR Jr (2017) Analytical solution of concentric two-pole Halbach cylinders as a preliminary design tool for magnetic refrigeration systems. J Magn Magn Mater 444:87–97
25. Fortkamp FP, Lang GB, Lozano JA, Barbosa JR Jr (2020) Design trade-offs for an active magnetic regenerator device. Appl Therm Eng 165:114467
26. Momen AM, Abdelaziz O, Gluesenkamp K, Vineyard E, Benedict M (2014) Thermofluid analysis of magnetocaloric refrigeration. In: Proceedings of the ASME (2014) international mechanical engineering congress and exposition. Montreal, Canada, November, p 2014
27. Zhang M, Abdelaziz O, Momen AM, Abu-Heiba A (2017) A numerical analysis of a magnetocaloric refrigerator with a 16-layer regenerator. Sci Rep 7:13962
28. Bouchekara HREH, Kedous-Lebouc A, Yonnet JP, Chillet C (2014) Multiobjective optimization of AMR systems. Int J Refrig 37:63–71
29. Ganjehsarabi H, Dincer I, Gungor A (2016) Analysis and optimisation of a cascade active magnetic regenerative refrigeration system. Int J Exergy 19:143–160
30. Roy S, Poncet S, Sorin M (2017) Sensitivity analysis and multiobjective optimization of a parallel-plate active magnetic regenerator using a genetic algorithm. Int J Refrig 75:276–285
31. Teyber R, Trevizoli PV, Christiaanse TV, Govindappa P, Niknia I, Rowe A (2017b) Permanent magnet design for magnetic heat pumps using total cost minimization. J Magn Magn Mater 442:87–96
32. Trevizoli PV, Nakashima AT, Barbosa JR Jr (2016b) Performance evaluation of an active magnetic regenerator for cooling applications part II: mathematical modeling and thermal losses. Int J Refrig 72:206–217

33. Nield DA, Bejan A (2006) Convection in porous media, 3rd edn. Springer, New York
34. Eriksen D, Engelbrecht K, Bahl CRH, Bjørk R, Nielsen KK (2016) Effects of flow balancing on active magnetic regenerator performance. Appl Therm Eng 103:1–8
35. Nielsen KK, Tusek J, Engelbrecht K, Schopfer S, Kitanovski A, Bahl CRH, Smith A, Pryds N, Poredos A (2011) Review on numerical modeling of active magnetic regenerators for room-temperature applications. Int J Refrig 34:603–616
36. Bahl CRH, Nielsen KK (2009) The effect of demagnetization on the magnetocaloric properties of gadolinium. J Appl Phys 105:013916
37. Klein SA (2013) EES—engineering equation solver, Professional Version v9.339. F-Chart Software, 2013. http://www.fchartsoftware.com
38. Lei T, Engelbrecht K, Nielsen KK, Veje CT (2017) Study of geometries of active magnetic regenerators for room temperature magnetocaloric refrigeration. Appl Therm Eng 111:1232–1243
39. Niknia I, Campbell O, Christiaanse TV, Govindappa P, Teyber R, Trevizoli PV, Rowe A (2016) Impacts of configuration losses on active magnetic regenerator device performance. Appl Therm Eng 106:601–612
40. Peixer GF, Lozano JA, Barbosa Jr JR (2017) Performance evaluation of AMRs using different casings. Book of Abstracts for the Danish Days on Caloric Materials and Devices
41. Neves Bez H, Nakashima ATD, Lang GB, Lozano JA, Barbosa Jr JR (2018) Numerical simulations and experimental tests of Gd-Y multi-layered active magnetic regenerators. In: Proceedings of the eighth IIR conference on caloric cooling (Thermag VIII), Darmstadt, Germany
42. Hermes CJL, Melo C (2008) A first-principles simulation model for the start-up and cycling transients of household refrigerators. Int J Refrig 31(8):1341–1357
43. Negrão COR, Hermes CJL (2011) Energy and cost savings in household refrigerating appliances: a simulation-based design approach. Appl Energy 88(9):3051–3060